A Method for Calculating Atmospheric Radiation Produced by Relativistic Electron Precipitation

Wei Xu[1], Robert A. Marshall[1], and W. Kent Tobiska[2]

[1]Department of Aerospace Engineering Sciences, University of Colorado Boulder, Boulder, CO, USA.
[2]Space Environment Technologies, Pacific Palisades, CA, USA.

Key Points:

- We report a lookup table of atmospheric radiation production between ground and low-Earth-orbit by monoenergetic precipitation electrons
- We explain how this lookup table can be utilized for rapid specification of radiation production by arbitrary precipitation energy spectrum
- We validate this lookup table by comparing with balloon measurements of X-ray spectrum in stratosphere during radiation belt precipitation

Corresponding author: Wei Xu, Wei-Xu@colorado.edu

Abstract

Radiation safety in the Earth's atmosphere is of particular importance to our living environment, especially at aviation altitudes. Aviation radiation has been long known to originate primarily from the galactic and solar system: galactic cosmic rays and solar energetic protons. Recent flight measurements by the Automated Radiation Measurements for Aerospace Safety (ARMAS) experiment have uncovered another potential source for aviation radiation: Relativistic Electron Precipitation (REP) from the Van Allen radiation belts. REP can induce radiation at aviation altitudes through bremsstrahlung X-ray production, which carries radiation down to the stratosphere and even the troposphere. In this study, using a suite of physics-based Monte Carlo models, we characterize the effective radiation dose produced at altitudes between ground and low-Earth-orbit by relativistic precipitation electrons with energies between 100 keV and 10 MeV. We produce a lookup table of atmospheric radiation production that calculates the expected radiation dose for a given precipitation flux, spectrum, and pitch angle distribution. This lookup table provides results that are consistent with X-ray measurements during radiation belt precipitation by balloon-borne instruments in the stratosphere, and can be directly used to convert space-borne measurements of precipitation fluxes into aviation radiation. This work represents our first attempt towards better understanding of REP's role in the atmospheric high-altitude radiation environment.

1 Introduction

Radiation from a number of sources can affect spacecraft in orbits ranging from low-Earth-orbit (LEO, 100–1000 km) to interplanetary space, as well as suborbital missions and high-altitude aircraft. The radiation exposure in the Earth's atmosphere increases in general with altitude above the surface, and aviation at higher altitudes is exposed to increasing radiation risk and exposure. Of particular importance is the radiation environment at commercial aviation altitudes: typically between 9.5 and 12.2 km (31,000 to 40,000 feet) above sea level [e.g., *Ruskin et al.*, 2008]. Aviation radiation has been long known to originate primarily from the galactic and solar system: Galactic Cosmic Rays (GCR) and Solar Energetic Particles (SEP) [e.g., *Vainio et al.*, 2009]. GCRs are believed to originate from diffusive shock acceleration in supernova remnants and consist mostly of protons and α particles [e.g., *Blandford and Eichler*, 1987]. SEPs, on the other hand, are caused by coronal mass ejections and/or solar flares [e.g., *Desai and Giacalone*, 2016], and consist mostly of protons and sometimes electrons and heavy ions [e.g., *Reames*, 1999]. Regardless of the origin and composition, after entering the atmosphere, both SEPs and GCRs strongly interact with neutral species and cascade into a cluster of energetic secondary particles. Depending on the initial energy, a fraction of secondary particles may penetrate into the stratosphere and troposphere, and cause human exposure to high linear energy transfer (LET) radiation at aircraft altitudes [*Wilson et al.*, 1995], possibly leading to nausea, acute sickness, cancer, and/or other irreversible health damage [*Vainio et al.*, 2009].

The radiation damage brought by GCR and SEP has been extensively studied via modeling and observational techniques [e.g., *Duggal*, 1979; *O'Brien et al.*, 1996; *Ferrari et al.*, 2001; *Vainio et al.*, 2009]. GCR intensity in general varies with the 11-year solar cycle due to modulation of the interplanetary magnetic field (IMF) generated by the sun [e.g., *Vainio et al.*, 2009]. A typical value of GCR background radiation at altitude of 10–15 km is approximately $1–10\times10^{-6}$ Sv/hr [e.g., *Mertens et al.*, 2013; *Tobiska et al.*, 2018]. *Copeland et al.* [2008] have investigated a total of 169 SEP events measured by the Geostationary Operational Environmental Satellite (GOES) between 1986 and 2008; the maximum radiation dose in one hour to an adult produced by GCR and SEP is found to be ~2.6 mSv at 18.3 km altitude. As for modeling studies, *Ferrari et al.* [2001] have performed detailed simulation of GCR transport in the atmosphere using the FLUKA code

[*Ferrari et al.*, 2005], and tabulated the effective dose rate as a function of geomagnetic cut-off and altitude. Using Monte Carlo simulation of cosmic-ray-induced atmospheric cascade, *Mishev* [2014] has also developed a numerical model for the computation of radiation dose due to cosmic rays with galactic and solar origin. More recently, another physics-based model, Nowcast of Atmospheric Ionizing Radiation for Aviation Safety (NAIRAS), has been developed by *Mertens et al.* [2013] for real-time prediction of dosimetric quantities at aviation altitudes due to GCR and SEP. This model has been well calibrated using measurements from the NASA Radiation Dosimetry Experiment (RaD-X) stratospheric balloon flight mission [*Mertens et al.*, 2016].

The influence of SEP on the Earth's radiation environment exhibits great variation depending on the incident energy spectrum, incoming direction, and the cutoff rigidity of the Earth's magnetic field [*Freier and Webber*, 1963; *Duggal*, 1979; *O'Brien et al.*, 1996; *Bütikofer et al.*, 2008; *Mishev*, 2014]. The increase of solar particle flux on 20 January 2005 was one of the most intense SEP events ever observed. *Bütikofer et al.* [2008] found that, because of this SEP event, the effective radiation dose at aircraft altitudes increased by several orders of magnitude at high geomagnetic latitudes with the largest exposure being 3 mSv/h at the south polar region. *Matthiä et al.* [2009] also estimated the radiation exposure of this event and found the dose rate to be up to ~2 mSv/hr at aviation altitudes in the Antarctic region, and ~0.1 mSv/hr for the northern hemisphere.

In addition to SEP and GCR, the Earth's atmosphere naturally emits high-energy radiation during thunderstorm activity. This includes bursts of gamma-rays emanated from intense lightning discharges, a phenomenon called Terrestrial Gamma-ray Flashes (TGFs) [e.g., *Fishman et al.*, 1994; *Smith et al.*, 2011], and Thunderstorm Ground Enhancements (TGEs), which are enhancements of relativistic electrons, gamma-rays, and neutron bursts [*Rutjes et al.*, 2017] observed during winter thunderstorms along the coast of Japan [*Bowers et al.*, 2017; *Enoto et al.*, 2017] or at high mountain areas during thunderstorm activity [e.g., *Chilingarian et al.*, 2010]. Considering the potential damage, a variety of studies have been devoted to assessing the radiation exposure produced during thunderstorm activity. The modeling work of *Dwyer et al.* [2010] has revealed that the radiation dose received by crew members could potentially reach as high as ~0.1 Sv with a duration less than 1 ms if an aircraft flies near the source region of TGFs. *Xu et al.* [2014] have quantified the radiation exposure due to X-ray emissions during natural cloud-to-ground lightning discharge and found that the maximum radiation dose that could be received at ground level is approximately 0.4 mSv.

Other than the sources listed above, recent flight measurements by the Automated Radiation Measurements for Aerospace Safety (ARMAS) experiment have uncovered another potential source for aviation radiation: Relativistic Electron Precipitation (REP) from the Van Allen radiation belts [*Tobiska et al.*, 2018]. The ARMAS campaign flies Teledyne radiation dosimeters on aircraft including the NASA Armstrong Flight Research Center's DC-8, ER-2 and G-III, National Oceanic and Atmospheric Administration's (NOAA) G-IV, National Science Foundation/National Center for Atmospheric Research's G-V, and Federal Aviation Agency's Bombardier Global 5000 [*Tobiska et al.*, 2016]. In over 100 events measured during ARMAS flights, the radiation doses at L-shells between 1.5 and 5 were notably higher than the GCR background (on average ~15% higher), while SEPs and thunderstorms have been clearly ruled out as potential sources of radiation [*Tobiska et al.*, 2018]. By approximating REP-induced radiation using a polynomial function, the authors also found that the observed radiation enhancement can be satisfactorily explained.

These ARMAS findings are not surprising in view of the well-known bremsstrahlung-induced ionization effects: when deflected by atmospheric species, relativistic precipitation electrons produce energetic X-rays via bremsstrahlung emission, these X-rays can propagate further into the atmosphere and ionize air molecules at altitudes considerably lower than those of direct impact ionization [e.g., *Berger and Seltzer*, 1972; *Frahm et al.*, 1997; *Artamonov et al.*, 2016; *Xu et al.*, 2018]. Although the parameterization method

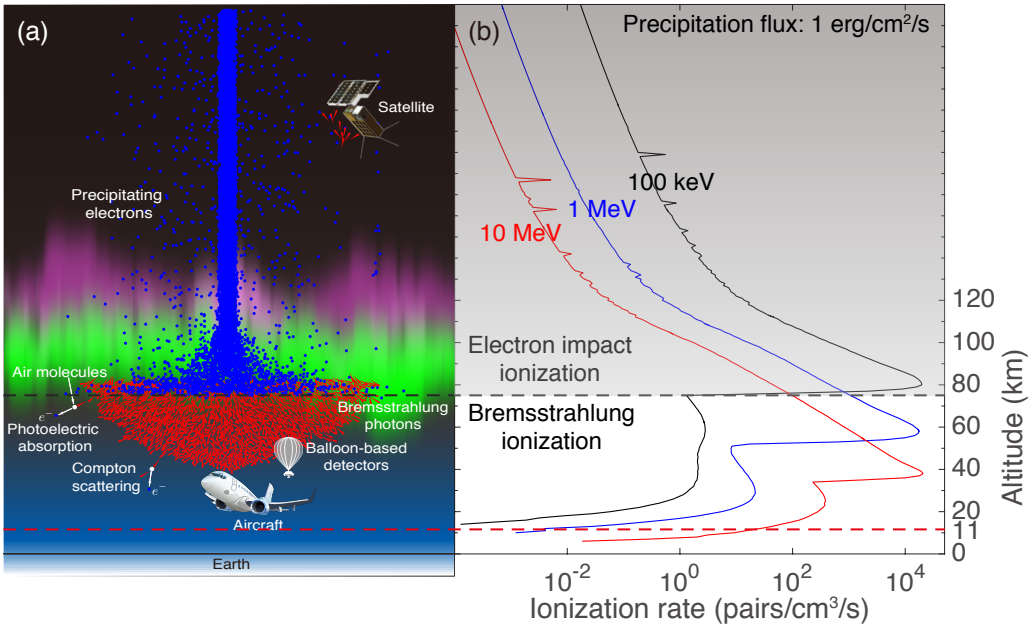

Figure 1. (a) Illustration of relativistic precipitation electrons and their cascade particles in the Earth's atmosphere, including bremsstrahlung photons, and photoelectrons and Compton electrons produced via photon collisions with neutral species. (b) Altitude profile of ionization production by monoenergetic beams of 100 keV, 1 MeV, and 10 MeV electrons. The source precipitation flux of each beam is 1 erg/cm^2/s. The black dashed line depicts the altitude below which the dominant ionization process transitions from direct impact ionization to bremsstrahlung-induced ionization for 100-keV precipitation electrons, while the red dashed line marks typical aviation altitudes (11 km). The horizontal spikes are numerical as caused by the energy deposition of a random particle in Monte Carlo simulations.

of *Fang et al.* [2008, 2010] does not explicitly include the bremsstrahlung effects, it has been suggested that the bremsstrahlung ionization could be significantly lower than the direct impact ionization. Figure 1a is a schematic view of relativistic precipitation electrons and their cascade particles in the Earth's atmosphere, including bremsstrahlung photons, and photoelectrons and Compton electrons produced via photon collisions with neutral species. Figure 1b shows the ionization production versus altitude by monoenergetic beams of 100 keV, 1 MeV, and 10 MeV electrons. These ionization profiles usually consist of two peaks, for example, the 10-MeV profile has a first peak at ~40 km altitude due to direct impact ionization by precipitation electrons, and a second peak at ~25 km due to bremsstrahlung-induced ionization. Of special interest to ARMAS measurements is the lowest altitude of bremsstrahlung ionization, which could be as low as 10 km for MeV precipitation electrons.

Thanks to the bremsstrahlung effects, various balloon experiments have been carried out to monitor REP events from the stratosphere, for example, the Balloon Array for Radiation belt Relativistic Electron Losses (BARREL) [*Millan et al.*, 2013] and the balloon observation by Lebedev Physical Institute [*Makhmutov et al.*, 2016]. Typical value of BARREL-measured X-ray fluxes during radiation belt precipitation is on the order of several thousand counts per second in the energy range between tens of keV and several MeV [*Woodger et al.*, 2015]. As for the balloon measurements at Lebedev Physical Institute, *Makhmutov et al.* [2016] fitted 20 years of balloon data using a precipitation source with an exponential energy distribution, and the characteristic (e-folding) energy was occasionally found to be as high as several tens of MeV indicating an appreciable flux of high-MeV electrons. Observations from both platforms converge to indicate that there exists intense X-ray flow in the stratosphere during REP, which can potentially reach troposphere and give rise to radiation exposure therein.

Given the importance of this radiation as described above, numerous models have been developed to predict aviation radiation due to GCR and SEP for forecasting/nowcasting purpose, and "*the need for continuing the development of physics-based models of the Earth's particle radiation environment*" has been emphasized in particular [*Vainio et al.*, 2009]. Nevertheless, the radiation production by REP is still hypothesized from tropospheric observations and not well understood. The lack of relevant studies motivates us to quantify the radiation dose brought by REP. In this study, we present Monte Carlo simulation of REP events, including bremsstrahlung effects; we calculate the effective radiation dose produced by monoenergetic beams of precipitation electrons; and we explain how these monoenergetic simulation results can be directly used for the specification of atmospheric radiation production by arbitrary REP spectra. This work represents our first attempt towards better understanding of REP's contribution to the atmospheric high-altitude radiation environment.

2 Model and Methodology

In this work, we simulate relativistic electron precipitation using two Monte Carlo models: the Energetic Precipitation Monte Carlo (EPMC) model [*Lehtinen et al.*, 1999] and the Monte Carlo model for Photons (MCP) [*Xu et al.*, 2012]. The main cascade particles of REP that give rise to radiation damage are bremsstrahlung photons, photoelectrons, and Compton electrons (photoelectrons and Compton electrons are denoted as secondary electrons hereafter). In this study, we mainly focus on the effective radiation dose originating from these particles at altitudes from ground level to LEO altitude (assumed to be 500 km in present study). Specifically, we perform a two-step simulation, similar to how REP was modeled in our previous studies [*Xu et al.*, 2018; *Xu and Marshall*, 2019]. The EPMC model is first employed to simulate the interaction of primary precipitation electrons with the Earth's atmosphere, including bremsstrahlung production. Second, we simulate the transport of bremsstrahlung photons obtained in the first step, as well as production of secondary electrons, using the MCP model. We have verified that the majority

of these secondary electrons cannot move more than one grid cell in altitude (1 km) and their transport in the atmosphere is therefore not simulated. In the following discussion, we introduce the numerical models and setup of the Monte Carlo simulations.

The EPMC model was originally developed by *Lehtinen et al.* [1999] at Stanford University for studies of energetic radiation from thunderstorm activity, and has been recently updated by our group at the University of Colorado Boulder to study REP [e.g., *Marshall et al.*, 2014; *Xu et al.*, 2018; *Marshall and Bortnik*, 2018]. This model utilizes the electron stopping power of atmospheric species and explicitly solves the equation of electron motion at the microscopic level. Angular diffusion is modeled using the method of small-angle collisions [*Lehtinen*, 2000, pp. 15–18]; this model can adopt an arbitrary background neutral density profile and magnetic field as input. In this work, the background magnetic field is assumed to be vertical with a magnitude of 41,528 nT; magnetic mirroring due to the magnetic gradient force is also included [*Lehtinen*, 2000, pp. 108–109]. The neutral density profile of the background atmosphere used in present simulations is obtained from the NRLMSISE-00 model [*Picone et al.*, 2002].

The MCP model simulates the dynamics and collisions of photons with energies from 10 keV to 100 MeV using experimentally-measured cross sections (see [*Xu et al.*, 2012] for more details). The main types of photon collisions in this energy range are: photoelectric absorption, Compton scattering, and electron-positron pair production. Pair production is the dominant collision process for photons with energies above ~30 MeV, and thus not important in the present study. We note that this set of Monte Carlo models (EPMC and MCP) has been employed in the past few years for a series of studies related to REP and lightning discharge; good agreements with previously published results, including GEANT4 simulations, and/or observation data have been obtained [e.g., *Xu et al.*, 2018; *Xu and Marshall*, 2019; *Marshall et al.*, 2019].

In this study, we simulate monoenergetic beams of precipitation electrons with sufficient energy to penetrate into the stratosphere; 20 energy values are used, logarithmically spaced between 100 keV and 10 MeV. Each monoenergetic beam is assumed to precipitate into the upper atmosphere from an initial altitude of 500 km; the source precipitation area is assumed to be a disc with 500 km radius [e.g., *Whittaker et al.*, 2013]. The specific choice of initial altitude is not critical as long as it is well above the collision area (below 100 km altitude) between precipitation electrons and the atmosphere; as will be shown later, the radiation dose at altitudes between 100 and 500 km is almost invariant (Figure 6). Following previous studies on the ionization production by precipitation electrons [e.g., *Lummerzheim*, 1992; *Fang et al.*, 2008, 2010], the angular distribution of these electrons is assumed to be isotropic between 0° and 90° pitch angle at the initial altitude. Note that the true pitch angle distribution of precipitation electrons is not well known since nearly all existing space-borne instruments can only resolve part of the loss cone angle [*Marshall and Bortnik*, 2018], and an isotropic pitch angle distribution is representative of auroral precipitation electrons [e.g., *Nesse Tyssøy et al.*, 2016].

For each monoenergetic beam, the source flux is chosen to be 10^4 el/cm^2/s, similar to measurements by the Detection of Electro-Magnetic Emissions Transmitted from Earthquake Regions (DEMETER) satellite [e.g., *Whittaker et al.*, 2013]. The specific choice of precipitation flux is not critical since, for a given precipitation energy, the radiation production in the atmosphere scales linearly with source flux. In this study, we use an altitude of 11 km to discuss the effects on aviation radiation induced by REP since this altitude is close to that of ARMAS flight.

We perform monoenergetic simulations in order to tabulate the atmospheric response in terms of radiation production to different precipitation energies at altitudes between 0 and 500 km with 1 km resolution. Following the radiation calculation described in *Dwyer et al.* [2010]; *Mishev and Usoskin* [2015, 2018], the effective radiation dose $E_0(z)$ can be

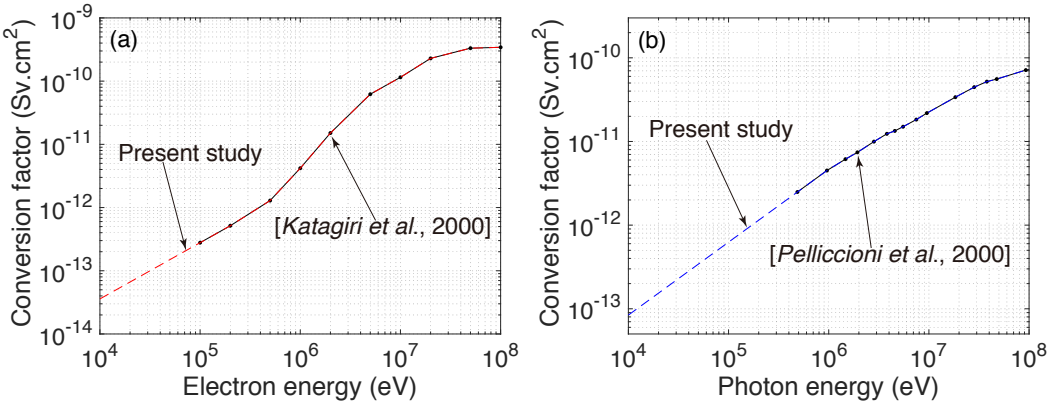

Figure 2. Fluence to radiation conversion factors for (a) electrons and (b) photons with energies between 10 keV and 100 MeV. Black solid lines with dots show the conversion factors for electrons and photons reported in *Katagiri et al.* [2000] and *Pelliccioni* [2000]. These factors are extrapolated, in the logarithmic energy scale, down to the minimum energy of present Monte Carlo simulations (10 keV) and shown as dashed lines.

computed using the particle flux and energy distribution at altitude z and a fluence-to-radiation conversion factor, with the following equation:

$$E_0(z) = \sum_i \phi(i,z) \int h(i,\varepsilon) f(i,\varepsilon,z) d\varepsilon \tag{1}$$

where i specifies the different particle types: $i = 1$, primary precipitation electrons; $i = 2$, bremsstrahlung photons; $i = 3$, secondary electrons. $\phi(i,z)$ is the mean flux (in units of particles/cm^2/s) of the i-th type of particle at altitude z, $h(i,\varepsilon)$ is the fluence to radiation conversion factor (in units of Sv cm^2) for the i-th type of particle with energy ε (see Figure 2), and $f(i,\varepsilon,z)$ is the corresponding energy distribution. The energy distribution is normalized so that the integration over energy yields unity: $\int f(i,\varepsilon,z)d\varepsilon = 1$; with this normalization, the integral term in equation 1 ($\int f(i,\varepsilon)h(i,\varepsilon)d\varepsilon$) calculates the average value of conversion factors for all the i-th type of particles at altitude z.

The particle flux $\phi(i,z)$ and energy distribution $f(i,\varepsilon,z)$ can be readily derived from EPMC and MCP simulations (see Figures 3–5). As a built-in feature, EPMC outputs, at prespecified physical times, the location, velocity, and energy of all electrons left in the simulation domain. As for MCP simulation, horizontal planes at discrete altitudes with 1 km step size between 0 and 500 km are assumed to be "virtual" detectors; we keep track of all the particles that cross these detectors' planes, including their velocity and location. After obtaining $\phi(i,z)$ and $f(i,\varepsilon,z)$, the resultant radiation dose can be explicitly calculated using equation 1 and fluence-to-radiation conversion factor $h(i,\varepsilon)$. Note that $h(i,\varepsilon)$ describes the potential radiation damage to the human body induced by unit particle fluence (flux integrated in time), whereas the output of the present Monte Carlo simulations is particle flux. Thus, we assume a duration of one hour for each monoenergetic simulation and calculate the rate of effective radiation dose in unit of Sv/hr.

The energy distribution at different altitudes is critical in equation 1 since the fluence to radiation conversion factor is highly energy dependent for both electrons and photons. Figure 2 shows the fluence to radiation conversion factors utilized in this study for electrons and photons with energies between 10 keV and 100 MeV. These factors are obtained from *Katagiri et al.* [2000] and *Pelliccioni* [2000] for electrons and photons, respec-

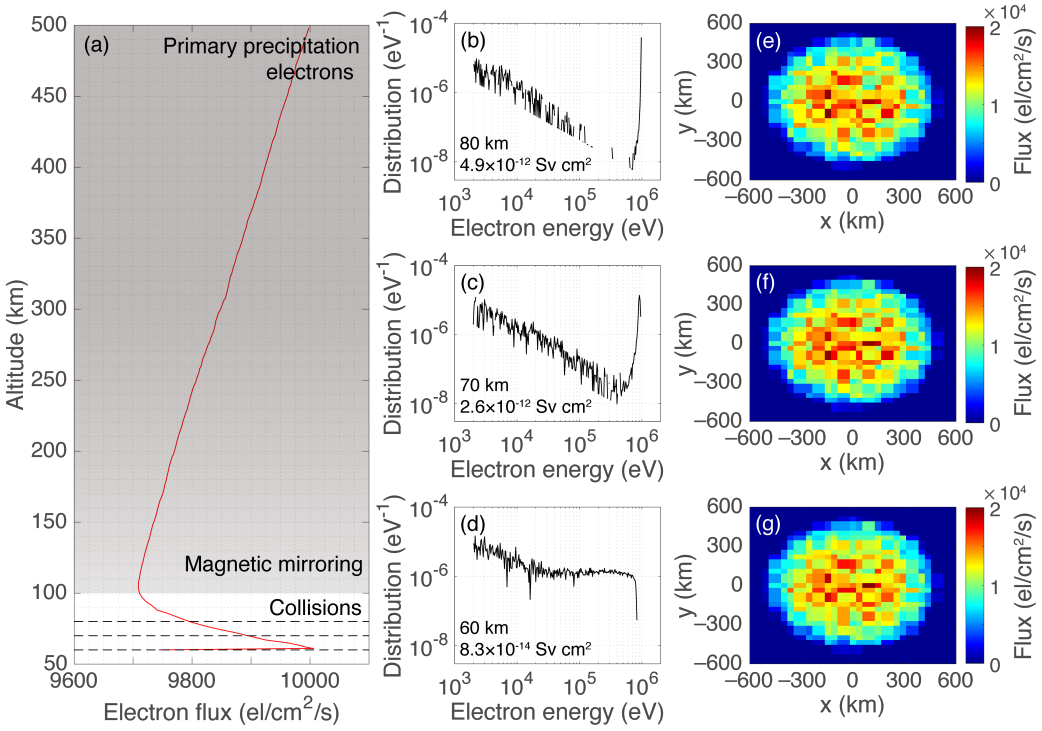

Figure 3. Primary precipitation electrons. (a) Flux of primary precipitation electrons versus altitude. The precipitation source is a monoenergetic beam of 1 MeV electrons with a flux of 10^4 el/cm^2/s; their pitch angle distribution is isotropic between 0° and 90° at 500 km altitude. The shaded area depicts the altitude range in which precipitation flux decreases due to magnetic mirroring force and the horizontal dashed lines mark the altitudes of 80, 70, and 60 km. Energy distribution of precipitation electrons at (b) 80 km, (c) 70 km, and (d) 60 km altitude. Spatial distribution of precipitation electrons at (e) 80 km, (f) 70 km, and (g) 60 km altitude.

tively, and correspond to the incident direction of anteroposterior (AP or front-to-back). The conversion factors reported in *Katagiri et al.* [2000] and *Pelliccioni* [2000] are mostly for energies above 100 keV (black solid lines and dots in Figure 2). For consistency, we extrapolate these factors in logarithmic energy scale down to the minimum energy of our Monte Carlo simulations (10 keV). The extrapolated conversion factors are shown as dashed lines in Figure 2.

In the following discussion, we use the monoenergetic beam of 1-MeV electrons as an example to showcase how the effective radiation dose from primary precipitation electrons, bremsstrahlung photons, and secondary electrons is obtained from EPMC and MCP simulations, in section 3.1. The lookup table of radiation production by precipitation electrons with energies from 100 keV to 10 MeV is presented in section 3.2. We explain in section 4 how this lookup table can be utilized to calculate the radiation dose produced by an arbitrary precipitation spectrum, and validate this lookup table in section 5 using BARREL measurements of X-ray spectra during radiation belt precipitation.

3 Lookup Table of Atmospheric Radiation Production

3.1 Monoenergetic Beam of 1-MeV Electrons

Figure 3 shows EPMC modeling results of 1 MeV precipitation electrons. Figure 3a shows the particle flux versus altitude when a monoenergetic beam of 1-MeV electrons is injected into the atmosphere from an initial altitude of 500 km. The source precipitation flux is 10^4 el/cm^2/s and the pitch angle distribution is isotropic between 0° and 90° at the initial altitude. The electron flux first decreases from 500 to ~100 km altitude as ~3% of precipitation electrons are mirrored back to the radiation belts due to the magnetic mirroring force. At altitudes below 100 km, neutral species become considerably denser, ionization collisions become more efficient, and the flux in turn increases. This sharp turn at 100 km is exactly the reference altitude typically used in the definition of bounce loss cone angle: the altitude below which radiation belt electrons are believed to start colliding with atmospheric species [*Marshall and Bortnik*, 2018].

The energy distribution of precipitation electrons at 80±5 km, 70±5 km, and 60±5 km altitude is shown in Figures 3b, 3c, and 3d, respectively. Figures 3e, 3f, and 3g show the corresponding spatial distribution at these altitudes, i.e., how precipitation electrons spread in lateral direction. The energy distribution at 80 km altitude (Figure 3b) peaks at the initial precipitation energy of 1 MeV and the tail at energies between 2 keV and several hundred keV corresponds to those electrons that are newly produced via ionization collisions. It is clear from the comparison between Figures 3b–3d that, due to atmospheric attenuation, the energy distribution gradually becomes softer as the precipitation beam propagates downward. In the lateral direction, the precipitation beam does not expand noticeably and electrons are mostly distributed within the source precipitation area (500 km radius).

Knowing the evolution of the energy distribution, we can calculate the average value of the conversion factors for primary electrons at each altitude step using the integral term in equation 1. These values are 4.9×10^{-12}, 2.6×10^{-12}, and 8.3×10^{-14} Sv cm^2 for the altitude of 80, 70, 60 km, respectively. Note that there might be some uncertainties in these conversion factors, which could be improved by using more particles in EPMC simulations. However, in our modeling, we compute these factors at every 1 km step. The conversion factor becomes smaller with decreasing altitude because, as electrons move downward, the fraction of high-energy electrons decreases, while the fraction of low-energy electrons increases (see Figures 3b–3d). The fluence to radiation conversion factor increases monotonically with electron energy (see Figure 2) and, thus, the average value of the conversion factor becomes smaller at lower altitudes.

Figure 4 shows MCP modeling results of bremsstrahlung photons. Figure 4a shows the spatial distribution of bremsstrahlung photons produced by the monoenergetic beam of 1 MeV electrons with a source flux of 10^4 el/cm^2/s. The color represents the flux of photons that would be measured by an isotropic observer at a given location. The dark red area at altitudes around 65 km is where bremsstrahlung photons are originally produced by precipitation electrons. A significant fraction of these photons is forward-emitted into the lower atmosphere and eventually absorbed at altitudes above 10 km, with a certain fraction being backscattered into the space. Figures 4b, 4c, and 4d show the energy distribution of bremsstrahlung photons at 70, 50, and 30 km, respectively. The energy distribution in Figure 4b represents those X-rays that are originally produced by 1-MeV electrons. Downward-propagating photons are heavily scattered and absorbed by the atmosphere, leading to the sharp drop at energies below ~30 keV, as evident in Figures 4e and 4f. Note that the simulated X-ray flux (Figure 4a) and spectrum (Figure 4d) at balloon altitudes (30–35 km) are strongly representative of BARREL X-ray observations during radiation belt precipitation [e.g., *Woodger et al.*, 2015; *Halford et al.*, 2015].

Figure 5 shows MCP modeling results of bremsstrahlung-induced secondary electrons. Figure 5a shows the normalized altitude distribution of photoelectrons and Compton

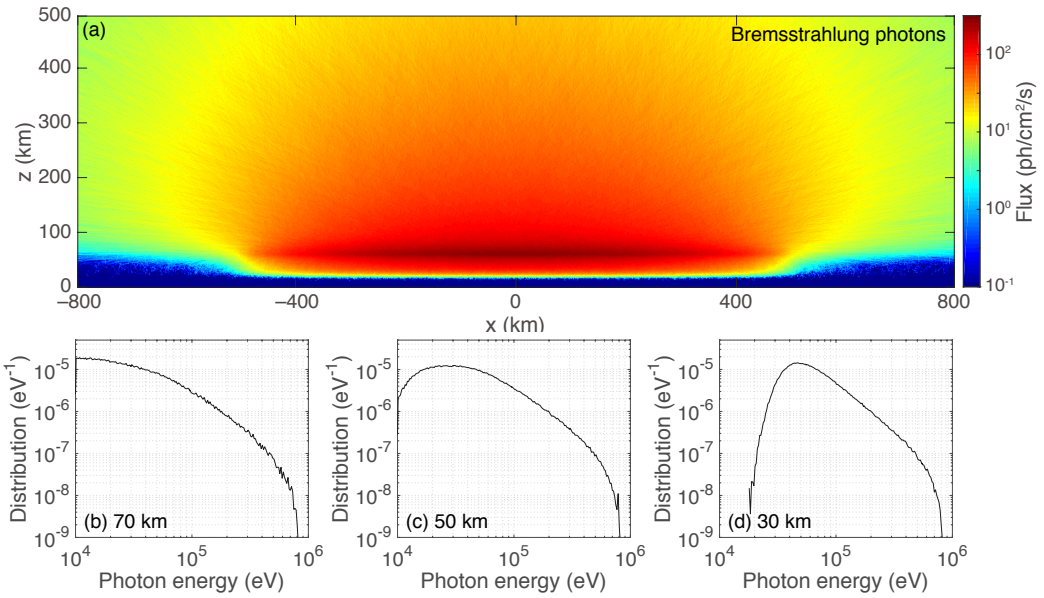

Figure 4. Bremsstrahlung photons. (a) Spatial distribution of bremsstrahlung photons produced by a monoenergetic beam of 1 MeV electrons. The source precipitation flux is 10^4 el/cm^2/s. Energy distribution of bremsstrahlung photons at (b) 70 km, (c) 50 km, and (d) 30 km altitude. These distributions are normalized so that the integration over energy yields unity.

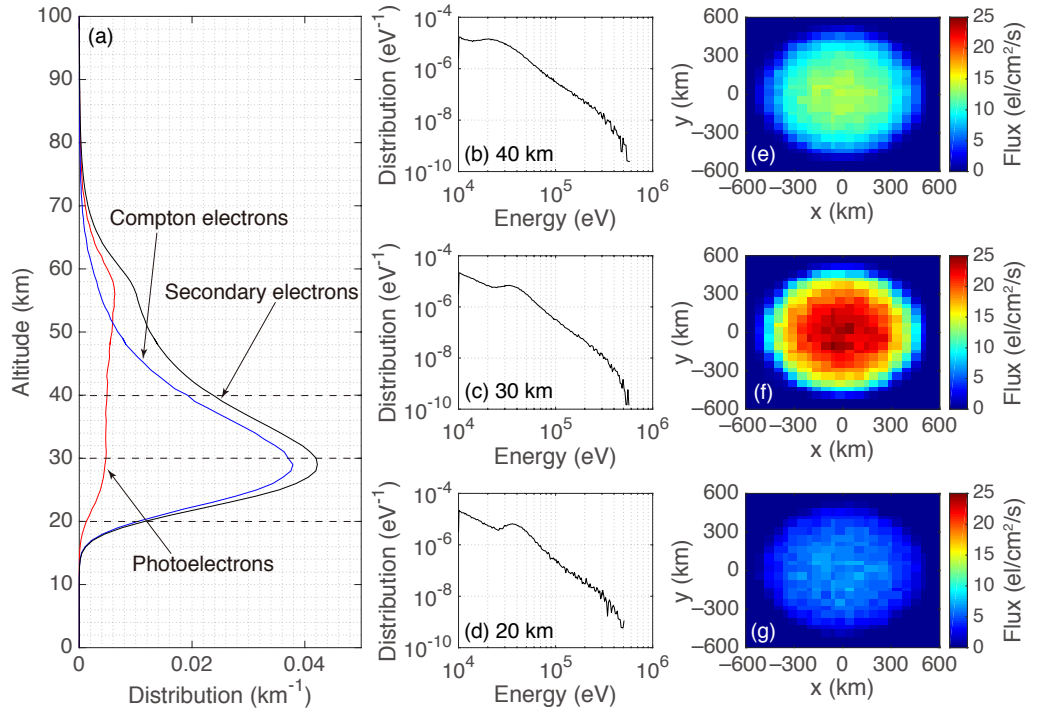

Figure 5. Secondary electrons. (a) Altitude distribution of photoelectrons and Compton electrons produced by bremsstrahlung photons originating from the monoenergetic beam of 1 MeV electrons. The source precipitation flux is 10^4 el/cm^2/s. Energy distribution of secondary electrons at (b) 60±5 km, (c) 35±5 km, and (d) 20±5 km altitude. Spatial distribution of secondary electrons at (e) 60±5 km, (f) 35±5 km, and (g) 20±5 km altitude.

electrons; the integration over altitude yields unity. Photoelectrons are mostly produced near ~57 km altitude, whereas Compton electrons are produced at considerably lower altitudes (~29 km altitude). The main reason is that Compton scattering is the main collision process at energies from 30 keV to 30 MeV, while photoelectric absorption dominates the energy range below 30 keV. Photons with higher energies can propagate further away from the source (larger mean free path) and Compton electrons are on average produced deeper in the atmosphere. Figures 5c, 5d and 5e show the energy distribution of secondary electrons at 40, 30, and 20 km altitude, respectively, while Figures 5e–5g show the corresponding spatial distribution. The energy distribution of secondary electrons is self-similar at altitudes between 20 and 40 km, and these electrons are also well distributed inside the source precipitation region. As such, the average value of fluence-to-radiation conversion factor does not change significantly in this altitude range and the effective radiation dose is mainly controlled by the flux of secondary electrons.

3.2 Altitude Profile of Radiation Production by Monoenergetic Precipitation Electrons

Similar to the 1-MeV case presented above, we have repeated this set of Monte Carlo simulations for other precipitation energies between 100 keV and 10 MeV; modeling results are shown in Figure 6. Figure 6a shows the effective radiation dose produced by primary precipitation electrons as a 2D (precipitation energy, altitude) color plot and Figure 6b shows the same results, but as a semi-logarithmic plot of effective radiation dose versus altitude. The curves in Figure 6b are color coded using the corresponding precipitation energy. Figures 6c–6d show the effective radiation dose due to bremsstrahlung photons, while Figures 6e–6f show those of secondary electrons.

The radiation dose of primary precipitation electrons is almost invariant at altitudes above 100 km since the atmosphere in this altitude range is too thin. Hence, the dose is indicative of the flux of primary electrons passing through each altitude step. The radiation dose at LEO altitude ranges from $\sim 6.4\times10^{-8}$ to $\sim 5.9\times10^{-3}$ Sv/hr for precipitation energies between 100 keV and 10 MeV. It is also interesting to observe that the lowest altitude of radiation production scales roughly linearly with the source precipitation energy in logarithmic scale. Precipitation electrons with energies less than 100 keV are absorbed or mirrored at altitudes above 83 km. As for 10 MeV electrons, the lowest altitude of radiation production is ~41 km with a dose rate of 3.2×10^{-3} Sv/hr.

The altitudes of peak radiation production in Figures 6c–6d correspond to where bremsstrahlung photons are originally produced by primary precipitation electrons. The maximum dose is approximately 5×10^{-9} Sv/hr at 84 km and 2.6×10^{-5} Sv/hr at 38 km for the precipitation energy of 100 keV and 10 MeV, respectively. The corresponding lowest altitude of radiation production is 16 and 5 km. In contrast, the radiation dose from secondary electrons (Figures 6e–6f) is overall one order of magnitude lower. In the 10-MeV case, the peak radiation dose produced by secondary electrons is $\sim 1\times10^{-6}$ Sv/hr at 25 km altitude, compared to 26×10^{-6} Sv/hr at 38 km altitude produced by bremsstrahlung photons. Note that the altitude scales used for these three sets of plots are different.

By summing the contribution from different particles, we have calculated the total radiation production, as shown in Figure 7. Figure 7a shows 2D (precipitation energy, altitude) color plot of effective radiation dose produced by monoenergetic electrons with energies between 100 keV and 10 MeV at altitudes between 0 and 120 km. Figure 7b shows the same results, but as semilogarithmic plots of effective radiation dose versus altitude. Figure 7c is a zoom-in view of the altitude range between 4 and 20 km. The horizontal dashed lines mark a typical aviation altitude of 11 km.

The sharp edge in these radiation profiles is similar to the transition of the dominant ionization processes in ionization profiles (Figure 1). Radiation production is due mainly to primary electrons above this edge, and to bremsstrahlung photons below this edge. Be-

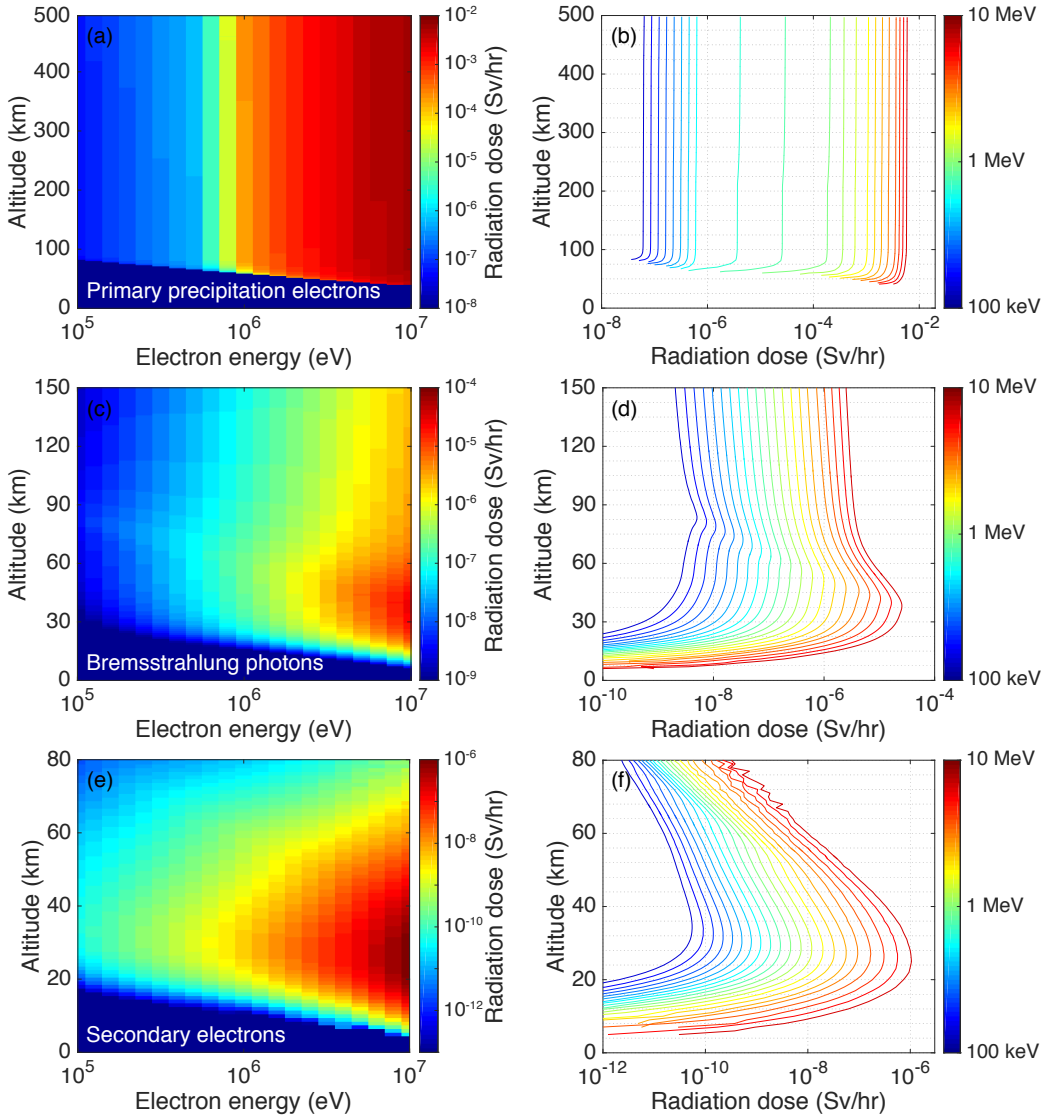

Figure 6. Effective radiation dose due to (a) primary precipitation electrons, (c) bremsstrahlung photons, and (e) secondary electrons produced by monoenergetic electrons with energies between 100 keV and 10 MeV. The source precipitation flux is assumed to be 10^4 el/cm^2/s for each monoenergetic beam. The right panels show the same results, but as semilogarithmic plots of effective radiation dose versus altitude.

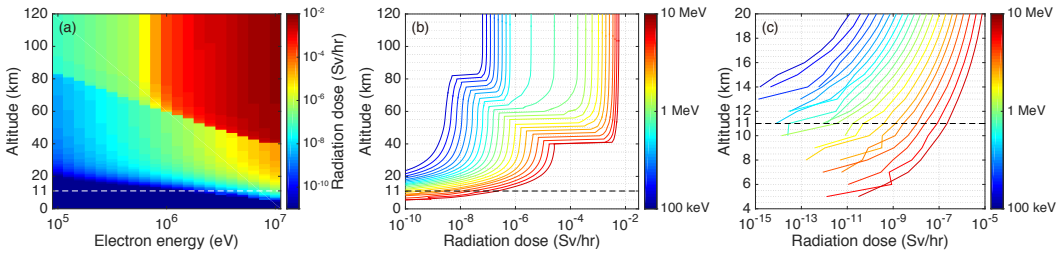

Figure 7. (a) Effective radiation dose produced by monoenergetic beams of electrons with energies between 100 keV and 10 MeV. The source precipitation flux is 10^4 el/cm^2/s. Panel (b) shows the same results, but as semilogarithmic plot of effective radiation dose versus altitude. Panel (c) is a zoom-in view of the radiation dose at altitudes between 4 and 20 km. The horizontal dashed lines mark a typical aviation altitude (11 km).

cause the fluence-to-radiation conversion factor is highly energy dependent, radiation production in the atmosphere does not scale proportionally as the total precipitation energy. For example, the radiation dose rate increases by almost five orders of magnitude as the precipitation energy changes from 100 keV to 10 MeV.

In regards to aviation radiation, the precipitation energy of electrons with energies below 1 MeV is completely absorbed at altitudes above 10 km and does not contribute to radiation doses below this altitude. The effective radiation dose produced by 2 and 10 MeV electrons at 11 km altitude is $\sim 5\times10^{-11}$ and $\sim 2.2\times10^{-7}$ Sv/hr, respectively. For reference, a typical value of GCR background radiation at this altitude is approximately 1–10×10^{-6} Sv/hr [e.g., *Tobiska et al.*, 2018]. It is important to emphasize that REP-induced radiation not only increases dramatically with precipitation energy, but altitude as well, as evidenced in Figure 7c. Using the 10-MeV profile as an example, the radiation dose at 11 km altitude is 2.2×10^{-7} Sv/hr and becomes 1.7×10^{-6} Sv/hr at 15 km altitude. With 4 km difference in altitude, the radiation dose rises by almost an order of magnitude and becomes comparable to GCR background radiation dose. This feature is particularly important for future high-altitude missions and aircraft flights.

4 Atmospheric Radiation Produced by Arbitrary Precipitation Spectra

The lookup table shown in Figure 7 is applicable to REP events with arbitrary energy spectra. Similar to how atmospheric ionization profiles are calculated using monoenergetic results [e.g., *Berger and Seltzer*, 1972; *Fang et al.*, 2010; *Xu et al.*, 2020], the altitude profile of effective radiation dose $E(z)$ can be computed by summing the contribution from each energy component using the following formula:

$$E(z) = \sum_{\varepsilon_{\min}}^{\varepsilon_{\max}} E_0(\varepsilon_{\mathrm{p}}, z) F(\varepsilon_{\mathrm{p}}) \Delta\varepsilon_{\mathrm{p}} \tag{2}$$

where $E_0(\varepsilon_{\mathrm{p}}, z)$ is the effective radiation dose (in units of Sv/hr) at altitude z produced by the precipitation energy of ε_{p}, $\varepsilon_{\min}$ and $\varepsilon_{\max}$ are the lowest and highest energy of precipitation spectrum, $F(\varepsilon_{\mathrm{p}})$ is the differential flux of precipitation electrons at different energies, and $\Delta\varepsilon_{\mathrm{p}}$ is the width of energy bins. In theory, REP-induced radiation production is not solely controlled by the precipitation energy spectrum, but also by the background magnetic field, the precipitation pitch angle distribution, and the atmospheric condition (i.e., mass density) as well [*Xu et al.*, 2020]. Due to the complexity of this problem, we only consider the energy dependence in our first-step study. A more complete characterization, taking the dependence on pitch angle, magnetic field, and atmospheric conditions into account, is left for our next-step study. Of note, the lookup table presented in this study is obtained using a source precipitation flux of 10^4 el/cm^2/s. Future calculations using real REP measurements need to be rescaled using the true precipitation flux.

5 Validation: Comparison with BARREL Measurements

To validate this lookup table, we compare with X-ray spectra measured by BARREL in the stratosphere, at typical altitudes of 30–40 km, approximately ~20 km above aviation aircraft. The comparison with three BARREL-measured precipitation events, published in *Halford et al.* [2015]; *Clilverd et al.* [2017]; *Li et al.* [2014] respectively, is shown in Figure 8. For the sake of comparison, the precipitation source used in our simulation is chosen to be the same as those in *Halford et al.* [2015]; *Clilverd et al.* [2017]; *Li et al.* [2014]. Specifically, the precipitation source is exponentially distributed in energy with a characteristic energy of 106 keV for Figure 8a, and 365 keV for Figure 8b. As for Figure 8c, we explicitly use the precipitation fluxes and spectrum calculated by *Li et al.* [2014, Figure 4]. Figure 8d shows the effective radiation dose produced by these three sources if the precipitation flux is 10^4 el/cm^2/s. These results are obtained by directly convolving the source

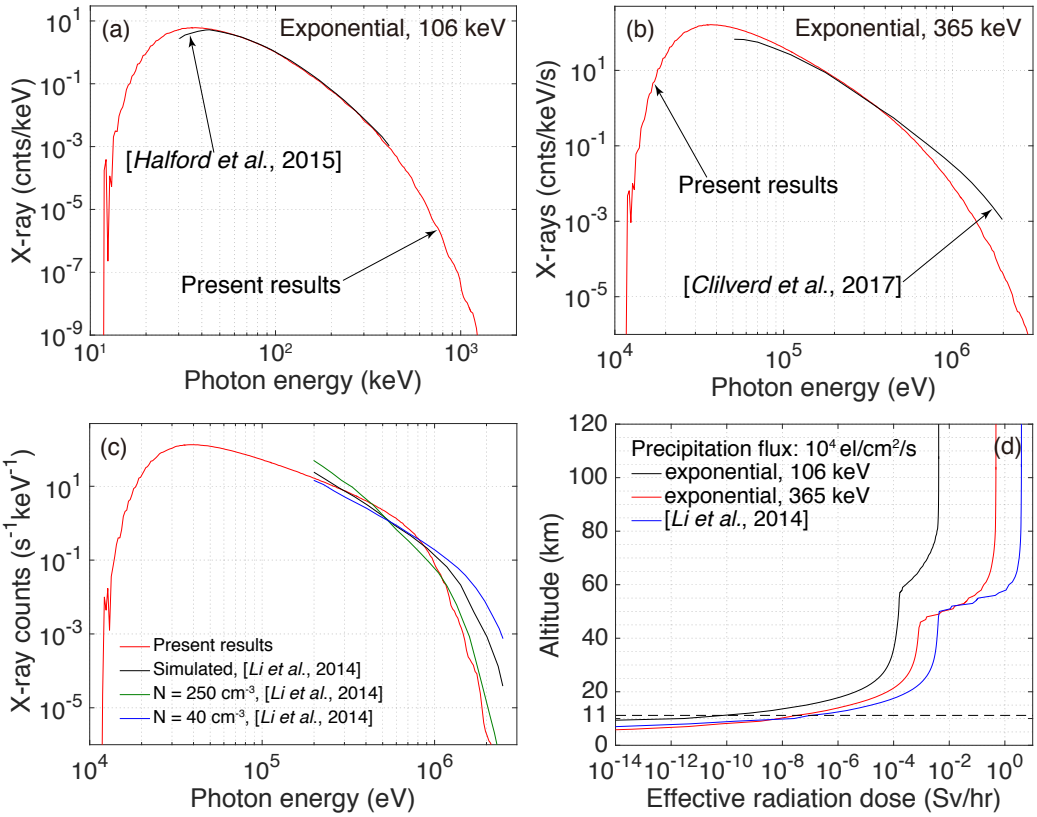

Figure 8. Comparison of X-ray spectra between present calculation and modeling studies of BARREL measurements reported in (a) *Halford et al.* [2015], (b) *Clilverd et al.* [2017], and (c) *Li et al.* [2014]. The precipitation source used in our REP simulation is an exponential distribution with a characteristic energy of 106 keV for panel a, and 365 keV for panel b, and the precipitation flux and spectrum calculated by *Li et al.* [2014] for panel c. (d) Lookup-table calculation of effective radiation dose produced by these three sources if the precipitation flux is 10^4 el/cm^2/s.

energy distribution with the lookup table presented in Figure 7, without performing Monte Carlo simulations. The stair-wise appearance of the red and blue curves at altitudes between ~45 and ~60 km is due to the discretization of energy steps we used for the lookup table.

The present results of X-ray spectra are in general consistent with previous modeling results [*Halford et al.*, 2015; *Clilverd et al.*, 2017; *Li et al.*, 2014], as well as BARREL measurements (not shown in Figure 8; close to the black curves). Our results show good agreement with *Halford et al.* [2015] at energies between 30 and 400 keV; our results also lie well within the X-ray spectra calculated by *Li et al.* [2014] for different altitudes. As for the comparison with *Clilverd et al.* [2017], the discrepancy at energies above 350 keV may be caused by: 1) the maximum energy of the precipitation source in our simulation (10 MeV) is lower than that used in *Clilverd et al.* [2017]; 2) the detector response is not included in present simulation; and 3) the background atmosphere of our Monte Carlo simulations may be different from that of *Clilverd et al.* [2017]. Note that the main purpose of Figure 8 is to compare the X-ray spectral shape/hardness since the source precipitation flux utilized by *Halford et al.* [2015]; *Clilverd et al.* [2017]; *Li et al.* [2014] to obtain consistent results with BARREL measurements was not explicitly given. Nevertheless, as shown in Figure 4, our modeling results of X-ray fluxes at balloon altitudes agree, at least within an order of magnitude, with BARREL measurements.

6 Discussion and Future Research

In this study, using two rigorous Monte Carlo models, we have simulated precipitation of relativistic electrons from the radiation belts, their interaction with atmospheric neutral species, and the resultant radiation production. A lookup table that fully describes the atmospheric radiation production at altitudes from the ground level up to LEO altitude has been calculated for precipitation electrons with energies between 100 keV and 10 MeV. Moreover, we explain how this lookup table can be employed for rapid specification of radiation production by an arbitrary precipitation spectrum.

This lookup table provides consistent results with X-ray measurements by BARREL during radiation belt precipitation events. As shown in Figure 8, for three precipitation events measured by BARREL, present results of X-ray spectra show good agreement with the modeling work reported in *Halford et al.* [2015]; *Clilverd et al.* [2017]; *Li et al.* [2014], as well as BARREL measurements. As such, this lookup table has been verified for the altitude range between balloon-borne platforms and LEO altitude. For better calibration, we plan on comparing directly with flight measurements at aviation altitudes, for example, ARMAS. However, such comparison requires high-resolution measurements of precipitation fluxes in the space and radiation dose at aviation altitudes with close correlation in space, time, and energy. This represents the goal of our next-step study.

An ARMAS flight on 03 October 2015 at 15–16 UT and 11.5 km altitude recorded enhanced radiation fluxes with the measured variable dose rate being a factor of up to two above normal GCR background levels; the GCR-subtracted dose rate is approximately 1–10 μSv/h. The ARMAS team (Tobiska, private communication) estimated that a 1-MeV photon fluence of 4.5×10^6 ph/cm^2 (with a duration of half an hour) was expected at this time based on Van-Allen-Probes-derived inputs of electron fluxes of 6×10^5 el/cm^2/s at 1 MeV and 2×10^2 el/cm^2/s at 5 MeV, and 7% of the electron flux being converted to 1 MeV bremsstrahlung photons. Our results indicate that a beam of 10 MeV electrons with a flux of 10^4 el/cm^2/s could result in a bremsstrahlung-generated dose rate of $\sim2.2\times10^{-7}$ Sv/hr at 11 km, and 4×10^{-7} Sv/hr at 12 km altitude.

To explain the ARMAS observation of $1–10\times10^{-6}$ Sv/hr at 11.5 km altitude on 03 October 2015, a precipitation flux of up to an order of magnitude above the model value is required. This is an extraordinarily high flux of 10 MeV electrons. SAMPEX, for ex-

ample, regularly measured fluxes of 10^5 electrons/cm^2/str/s of energies greater than 1 MeV [e.g., *Baker et al.*, 1994]. If fitted using an exponential function, the e-folding energy of SAMPEX measurements is found to be between ~70 keV and ~1.4 MeV [*Comess et al.*, 2013]. A flux of 10^5 el/cm^2/str/s at 1 MeV corresponds to a flux of ~161 el/cm^2/str/s at 10 MeV if we assume an e-folding energy of 1.4 MeV for the precipitation fluxes. On the other hand, balloon measurements reported in *Makhmutov et al.* [2016] show that the e-folding energy could be sometimes as high as several tens of MeV and, in this extreme case, the precipitation flux at 10 MeV becomes closer to what is needed to explain ARMAS measurements. However, this only represents an order of magnitude comparison with ARMAS data and more detailed comparison needs to be performed in order to determine if the radiation enhancement measured by ARMAS could indeed be caused by REP.

According to the National Council on Radiation Protection and Measurements, aircrew have the highest average annual effective dose of 3.07 mSv among all radiation-exposed workers in the United States [*Schauer*, 2009]. The International Commission on Radiological Protection (ICRP) recommends effective dose limits of 20 mSv/year for radiation workers and 1 mSv/year for the public [*Wrixon*, 2008]. The dose limits recommended by the European Union is 6 mSv/year for aircrew and 2 mSv/year for the public [*Thierfeldt et al.*, 2009]. Present results show that the REP-induced radiation dose at aircraft altitude inside the precipitation area could be as high as 4×10^{-7} Sv/hr, as produced by 10 MeV precipitation electrons with a flux of 10^4 el/cm^2/s. In reality, precipitation flux could be amplified by orders of magnitude and the precipitation spectrum varies rapidly due to repetitive wave-particle interactions. More importantly, as shown in Figure 7, REP-produced radiation dose increases sharply with altitude. Changing the source pitch angle distribution or background atmospheric density profiles could shift the radiation curves (Figure 7) up or down by 1–2 km, which can dramatically change the radiation dose at aviation altitudes due to the sharpness of these radiation curves. Therefore, to forecast/nowcast the potential radiation damage, one needs to rapidly convert real-time precipitation measurements and calculate the altitude profile of effective radiation dose. The lookup table reported here is developed to fulfill this need.

Radiation from REP will add to other well-known sources of radiation at aviation altitudes, i.e., SEP and GCR. GCRs impact the Earth's atmosphere everywhere around the globe, with a small variation with solar cycle due to the interplanetary magnetic field, and a significant variation with latitude, due to shielding by the Earth's magnetic field. SEPs impact the atmosphere mostly in the polar regions, entering the magnetosphere on open field lines. The minimum latitude that SEPs can reach depends on magnetospheric activity, leading to a cutoff latitude based on magnetic rigidity [e.g., *Smart and Shea*, 2005]. During solar proton events when SEPs are emitted from the sun in the direction of the Earth, operational models are used to divert air traffic to lower latitudes, avoiding the radiation exposure of SEPs. However, radiation belt precipitation occurs at latitudes just below where SEPs are incident, so traffic is essentially being rerouted directly into this radiation source. It is from this consideration that we suggest future studies take the spatial and temporal variation into account, and aim at assessing REP-induced radiation dose versus altitude, latitude, and longitude under different solar wind driving conditions using measurements from observation platforms in the stratosphere and/or space.

Acknowledgments

This research was supported by the NSF grant AGS-1732359 and NASA grant 80NSSC19K0648. W. K. Tobiska's research was supported by the NASA SBIR contract 80NSSC19C0194. The simulation data and analysis codes used to generate all figures and results in this paper, as well as the lookup table of effective radiation dose produced by monoenergetic electrons, are available at https://doi.org/10.5281/zenodo.4491211.

References

Artamonov, A. A., A. L. Mishev, and I. G. Usoskin (2016), Model CRAC: EPII for atmospheric ionization due to precipitating electrons: Yield function and applications, *J. Geophys. Res. Space Physics*, *121*, 1736–1743.

Baker, D., J. Blake, L. Callis, J. Cummings, D. Hovestadt, S. Kanekal, B. Klecker, R. Mewaldt, and R. Zwickl (1994), Relativistic electron acceleration and decay time scales in the inner and outer radiation belts: Sampex, *Geophysical research letters*, *21*(6), 409–412.

Berger, M. J., and S. M. Seltzer (1972), Bremsstrahlung in the atmosphere, *J. Atmos. Terr. Phys.*, *34*(1), 85–108.

Blandford, R., and D. Eichler (1987), Particle acceleration at astrophysical shocks: A theory of cosmic ray origin, *Physics Reports*, *154*(1), 1–75.

Bowers, G. S., D. M. Smith, G. F. Martinez-McKinney, M. Kamogawa, S. A. Cummer, J. R. Dwyer, D. Wang, M. Stock, and Z. Kawasaki (2017), Gamma ray signatures of neutrons from a terrestrial gamma ray flash, *Geophysical Research Letters*, *44*(19), 10,063–10,070, doi:https://doi.org/10.1002/2017GL075071.

Bütikofer, R., E. Flückiger, L. Desorgher, and M. Moser (2008), The extreme solar cosmic ray particle event on 20 january 2005 and its influence on the radiation dose rate at aircraft altitude, *Science of the total environment*, *391*(2-3), 177–183.

Chilingarian, A., A. Daryan, K. Arakelyan, A. Hovhannisyan, B. Mailyan, L. Melkumyan, G. Hovsepyan, S. Chilingaryan, A. Reymers, and L. Vanyan (2010), Ground-based observations of thunderstorm-correlated fluxes of high-energy electrons, gamma rays, and neutrons, *Phys. Rev. D*, *82*, 043,009, doi:10.1103/PhysRevD.82.043009.

Clilverd, M. A., C. J. Rodger, M. McCarthy, R. Millan, L. W. Blum, N. Cobbett, J. B. Brundell, D. Danskin, and A. J. Halford (2017), Investigating energetic electron precipitation through combining ground-based, and balloon observations, *J. Geophys. Res. Space Physics*, *122*, 534–546, doi:10.1002/2016JA022812.

Comess, M. D., D. M. Smith, R. S. Selesnick, R. M. Millan, and J. G. Sample (2013), Duskside relativistic electron precipitation as measured by sampex: A statistical survey, *Journal of Geophysical Research: Space Physics*, *118*(8), 5050–5058.

Copeland, K., H. H. Sauer, F. E. Duke, and W. Friedberg (2008), Cosmic radiation exposure of aircraft occupants on simulated high-latitude flights during solar proton events from 1 january 1986 through 1 january 2008, *Advances in Space Research*, *42*(6), 1008–1029.

Desai, M., and J. Giacalone (2016), Large gradual solar energetic particle events, *Living Reviews in Solar Physics*, *13*(1), 1–132.

Duggal, S. (1979), Relativistic solar cosmic rays, *Reviews of Geophysics*, *17*(5), 1021–1058.

Dwyer, J., D. Smith, M. Uman, Z. Saleh, B. Grefenstette, B. Hazelton, and H. Rassoul (2010), Estimation of the fluence of high-energy electron bursts produced by thunderclouds and the resulting radiation doses received in aircraft, *Journal of Geophysical Research: Atmospheres*, *115*(D9).

Enoto, T., Y. Wada, Y. Furuta, K. Nakazawa, T. Yuasa, K. Okuda, K. Makishima, M. Sato, Y. Sato, T. Nakano, et al. (2017), Photonuclear reactions triggered by lightning discharge, *Nature*, *551*(7681), 481–484.

Fang, X., C. E. Randall, D. Lummerzheim, S. C. Solomon, M. J. Mills, D. R. Marsh, C. H. Jackman, W. Wang, and G. Lu (2008), Electron impact ionization: A new parameterization for 100 eV to 1 MeV electrons, *J. Geophys. Res.*, *113*, A09311.

Fang, X., C. E. Randall, D. Lummerzheim, W. Wang, G. Lu, S. C. Solomon, and R. A. Frahm (2010), Parameterization of monoenergetic electron impact ionization, *Geophys. Res. Lett.*, *37*, L22106, doi:10.1029/2010GL045406.

Ferrari, A., M. Pelliccioni, and T. Rancati (2001), Calculation of the radiation environment caused by galactic cosmic rays for determining air crew exposure, *Radiation protection*

dosimetry, *93*(2), 101–114.

Ferrari, A., P. R. Sala, A. Fasso, J. Ranft, U. Siegen, et al. (2005), FLUKA: a multi-particle transport code, *Tech. rep.*, Stanford Linear Accelerator Center (SLAC).

Fishman, G. J., et al. (1994), The first BATSE gamma-ray burst catalog, *Astrophys. J. Suppl.*, *92*, 229–283, doi:10.1086/191968.

Frahm, R. A., J. D. Winningham, J. R. Sharber, R. Link, G. Crowley, E. E. Gaines, D. L. Chenette, B. J. Anderson, and T. A. Potemra (1997), The diffuse aurora: A significant source of ionization in the middle atmosphere, *J. Geophys. Res.*, *102*(D23), 28,203–28,214, doi:10.1029/97JD02430.

Freier, P., and W. Webber (1963), Exponential rigidity spectrums for solar-flare cosmic rays, *Journal of Geophysical Research*, *68*(6), 1605–1629.

Halford, A. J., et al. (2015), BARREL observations of an ICME-shock impact with the magnetosphere and the resultant radiation belt electron loss, *J. Geophys. Res. Space Physics*, *120*, 2557–2570, doi:10.1002/2014JA020873.

Katagiri, M., M. Hikoji, M. Kitaichi, S. Sawamura, and Y. Aoki (2000), Effective doses and organ doses per unit fluence calculated for monoenergetic 0.1 mev to 100 mev electrons by the mird-5 phantom, *Radiation protection dosimetry*, *90*(4), 393–401.

Lehtinen, N. G. (2000), Relativistic runaway electrons above thunderstorms, Ph.D. thesis, Stanford Univ., Stanford, CA.

Lehtinen, N. G., T. F. Bell, and U. S. Inan (1999), Monte Carlo simulation of runaway MeV electron breakdown with application to red sprites and terrestrial gamma ray flashes, *J. Geophys. Res.*, *104*(A11), 24,699–24,712, doi:10.1029/1999JA900335.

Li, Z., R. M. Millan, M. K. Hudson, L. A. Woodger, D. M. Smith, Y. Chen, R. Friedel, J. V. Rodriguez, M. J. Engebretson, J. Goldstein, et al. (2014), Investigation of EMIC wave scattering as the cause for the BARREL 17 January 2013 relativistic electron precipitation event: A quantitative comparison of simulation with observations, *Geophysical Research Letters*, *41*(24), 8722–8729.

Lummerzheim, D. (1992), Comparison of energy dissipation functions for high energy auroral electron and ion precipitation, *Rep. UAG-R-318*, pp. Geophys. Inst., Univ. of Alaska Fairbanks, Fairbanks.

Makhmutov, V., G. Bazilevskaya, Y. I. Stozhkov, A. Svirzhevskaya, and N. Svirzhevsky (2016), Catalogue of electron precipitation events as observed in the long-duration cosmic ray balloon experiment, *Journal of Atmospheric and Solar-Terrestrial Physics*, *149*, 258–276.

Marshall, R. A., and J. Bortnik (2018), Pitch Angle Dependence of Energetic Electron Precipitation: Energy Deposition, Backscatter, and the Bounce Loss Cone, *J. Geophys. Res. Space Physics*, *123*, 2412–2423.

Marshall, R. A., M. Nicolls, E. Sanchez, N. G. Lehtinen, and J. Neilson (2014), Diagnostics of an artificial relativistic electron beam interacting with the atmosphere, *J. Geophys. Res. Space Physics*, *119*, 8560–8577.

Marshall, R. A., W. Xu, A. Sousa, M. McCarthy, and R. Millan (2019), X-ray signatures of lightning-induced electron precipitation, *Journal of Geophysical Research: Space Physics*, *124*(12), 10,230–10,245.

Matthiä, D., B. Heber, G. Reitz, M. Meier, L. Sihver, T. Berger, and K. Herbst (2009), Temporal and spatial evolution of the solar energetic particle event on 20 january 2005 and resulting radiation doses in aviation, *Journal of Geophysical Research: Space Physics*, *114*(A8).

Mertens, C. J., M. M. Meier, S. Brown, R. B. Norman, and X. Xu (2013), NAIRAS aircraft radiation model development, dose climatology, and initial validation, *Space Weather*, *11*(10), 603–635.

Mertens, C. J., G. P. Gronoff, R. B. Norman, B. M. Hayes, T. C. Lusby, T. Straume, W. K. Tobiska, A. Hands, K. Ryden, E. Benton, et al. (2016), Cosmic radiation dose measurements from the RaD-X flight campaign, *Space Weather*, *14*(10), 874–898.

Millan, R. M., et al. (2013), The balloon array for RBSP relativistic electron losses (BARREL), *Space Sci. Rev.*, *179*, 503–530, doi:10.1007/s11214-013-9971-z.

Mishev, A. (2014), Computation of radiation environment during ground level enhancements 65, 69 and 70 at equatorial region and flight altitudes, *Advances in Space Research*, *54*(3), 528–535.

Mishev, A., and I. Usoskin (2015), Numerical model for computation of effective and ambient dose equivalent at flight altitudes-Application for dose assessment during GLEs, *Journal of Space Weather and Space Climate*, *5*, A10.

Mishev, A. L., and I. G. Usoskin (2018), Assessment of the radiation environment at commercial jet-flight altitudes during GLE 72 on 10 September 2017 using neutron monitor data, *Space Weather*, *16*(12), 1921–1929.

Nesse Tyssøy, H., M. I. Sandanger, L.-K. Ødegaard, J. Stadsnes, A. Aasnes, and A. Zawedde (2016), Energetic electron precipitation into the middle atmosphere–Constructing the loss cone fluxes from MEPED POES, *J. Geophys. Res. Space Physics*, *121*, 5693–5707.

O'Brien, K., W. Friedberg, H. H. Sauer, and D. Smart (1996), Atmospheric cosmic rays and solar energetic particles at aircraft altitudes, *Environment international*, *22*, 9–44.

Pelliccioni, M. (2000), Overview of fluence-to-effective dose and fluence-to-ambient dose equivalent conversion coefficients for high energy radiation calculated using the FLUKA code, *Radiat. Protect. Dosimetry*, *88*, 279–297.

Picone, J. M., A. E. Hedin, D. P. Drob, and A. C. Aikin (2002), NRLMSISE-00 empirical model of the atmosphere: Statistical comparisons and scientific issues, *J. Geophys. Res.*, *107*(A12), 1468, doi:10.1029/2002JA009430.

Reames, D. V. (1999), Particle acceleration at the sun and in the heliosphere, *Space Science Reviews*, *90*(3-4), 413–491.

Ruskin, K. J., K. A. Hernandez, P. G. Barash, and B. Riou (2008), Management of in-flight medical emergencies, *The Journal of the American Society of Anesthesiologists*, *108*(4), 749–755.

Rutjes, C., G. Diniz, I. S. Ferreira, and U. Ebert (2017), TGF Afterglows: A New Radiation Mechanism From Thunderstorms, *Geophysical Research Letters*, *44*(20), 10,702–10,712, doi:https://doi.org/10.1002/2017GL075552.

Schauer, D. (2009), Ionizing radiation exposure of the population of the united states, *The National Council on Radiation Protection and Measurements (NCRP), Report*, *160*.

Smart, D., and M. Shea (2005), A review of geomagnetic cutoff rigidities for earth-orbiting spacecraft, *Advances in Space Research*, *36*(10), 2012–2020.

Smith, D. M., et al. (2011), A terrestrial gamma ray flash observed from an aircraft, *Journal of Geophysical Research: Atmospheres*, *116*, D20124, doi:https://doi.org/10.1029/2011JD016252.

Thierfeldt, S., C. Haider, P. Hans, M. Kaleve, and F. Neuenfeldt (2009), Evaluation of the implementation of radiation protection measures for aircrew in eu member states, *Radiation protection dosimetry*, *136*(4), 324–328.

Tobiska, W. K., D. Bouwer, D. Smart, M. Shea, J. Bailey, L. Didkovsky, K. Judge, H. Garrett, W. Atwell, B. Gersey, et al. (2016), Global real-time dose measurements using the automated radiation measurements for aerospace safety (armas) system, *Space Weather*, *14*(11), 1053–1080.

Tobiska, W. K., L. Didkovsky, K. Judge, S. Weiman, D. Bouwer, J. Bailey, B. Atwell, M. Maskrey, C. Mertens, Y. Zheng, et al. (2018), Analytical representations for characterizing the global aviation radiation environment based on model and measurement databases, *Space Weather*, *16*(10), 1523–1538.

Vainio, R., L. Desorgher, D. Heynderickx, M. Storini, E. Flückiger, R. B. Horne, G. A. Kovaltsov, K. Kudela, M. Laurenza, S. McKenna-Lawlor, et al. (2009), Dynamics of the Earth's particle radiation environment, *Space science reviews*, *147*(3-4), 187–231.

Whittaker, I. C., R. J. Gamble, C. J. Rodger, M. A. Clilverd, and J.-A. Sauvaud (2013), Determining the spectra of radiation belt electron losses: Fitting DEMETER electron

flux observations for typical and storm times, *J. Geophys. Res. Space Physics*, *118*, 7611–7623, doi:10.1002/2013JA019228.

Wilson, J. W., J. E. Nealy, F. A. Cucinotta, J. L. Shinn, F. Hajnal, M. Reginatto, and P. Goldhagen (1995), Radiation safety aspects of commercial high-speed flight transportation, *NASA Technical Paper*, p. 3524.

Woodger, L. A., A. J. Halford, R. M. Millan, M. P. McCarthy, D. M. Smith, G. S. Bowers, J. G. Sample, B. R. Anderson, and X. Liang (2015), A summary of the BARREL campaigns: Technique for studying electron precipitation, *J. Geophys. Res. Space Physics*, *120*, 4922–4935, doi:10.1002/2014JA020874.

Wrixon, A. D. (2008), New icrp recommendations, *Journal of radiological protection*, *28*(2), 161.

Xu, W., and R. A. Marshall (2019), Characteristics of Energetic Electron Precipitation Estimated from Simulated Bremsstrahlung X-ray Distributions, *J. Geophys. Res. Space Physics*, *124*, 2831–2843.

Xu, W., S. Celestin, and V. P. Pasko (2012), Source altitudes of terrestrial gamma-ray flashes produced by lightning leaders, *Geophys. Res. Lett.*, *39*, L08801, doi:10.1029/2012GL051351.

Xu, W., S. Celestin, and V. P. Pasko (2014), Modeling of X-ray emissions produced by stepping lightning leaders, *Geophys. Res. Lett.*, *41*, 7406–7412, doi:10.1002/2014GL061163.

Xu, W., R. A. Marshall, X. Fang, E. Turunen, and A. Kero (2018), On the Effects of Bremsstrahlung Radiation During Energetic Electron Precipitation, *Geophys. Res. Lett.*, *45*(2), 1167–1176.

Xu, W., R. A. Marshall, H. N. Tyssøy, and X. H. Fang (2020), A generalized method for calculating atmospheric ionization by energetic electron precipitation, *Journal of Geophysical Research: Space Physics*, p. e2020JA028482.